Automated conformal mesh generation chain for woven composites based on CT-scan images with low contrasts

Guillaume Fourrier, Alain Rassineux, François-Henri Leroy, Martin Hirsekorn, Christian Fagiano, Emmanuel Baranger

Highlights

Automated conformal mesh generation chain for woven composites based on CT-scan images with low contrasts

Guillaume Fourrier, Alain Rassineux, François-Henri Leroy, Martin Hirsekorn, Christian Fagiano, Emmanuel Baranger

- Creation of conformal tetrahedral meshes of woven composites from μCT-scans
- Automated segmentation dealing with reconstruction artifacts and low contrast images
- Application to a material with fiber disorientation and yarn splitting defects

Automated conformal mesh generation chain for woven composites based on CT-scan images with low contrasts

Guillaume Fourrier[a,b,c], Alain Rassineux[b], François-Henri Leroy[a], Martin Hirsekorn[a], Christian Fagiano[a], Emmanuel Baranger[c]

[a] *DMAS, ONERA, Université Paris Saclay, 92322 Châtillon, France,*
[b] *Laboratoire Roberval, Université de Technologie de Compiègne, Centre de recherche Royallieu, CS 60319, 60203 Compiègne Cedex, France,*
[c] *Université Paris-Saclay, CentraleSupélec, ENS Paris-Saclay, CNRS, Laboratoire de Mécanique Paris-Saclay, 91190, Gif-sur-Yvette, France,*

Abstract

A novel approach to generate conformal meshes of woven composites at the mesoscopic scale from low-contrast CT-scan images with reconstruction artifacts is presented. The segmentation of the CT-scans relies on texture analysis of the tomography to differentiate the orientations of warp and weft yarns. The yarn paths are tracked through the scanned volume starting from the relative positions of the yarns on the external faces of the scanned volume. These paths provide seeds for a growing algorithm that labels the yarns in the initial voxelized mesh. The final conformal mesh is generated using smoothing and coarsening algorithms. The presented approach is mostly automated and allows generating quality controlled meshes suitable for finite element analyses with limited user intervention. Its flexibility is demonstrated by an application to a woven composite with manufacturing defects (fiber disorientation and yarn splitting).

Keywords: Woven Composites, Computed tomography segmentation, Mesoscopic scale, Manufacturing defects

1. Introduction

Thermoplastic composites are increasingly used in the aeronautic industry for numerous applications. Their thermoforming capability, and the absence of curing step [1] offers the possibility of automated processes, which is a major goal in order to reduce costs and

improve production rates. However, the process automation may create defects like local tow disorientations in the pieces. These defects can impair the material strength of structures. Modeling tools are therefore needed to gain a better understanding of the impact of these defects on the mechanical behavior.

Composite materials are modelled at three distinct scales : the microscopic scale, at which fibers and matrix are treated separately, the mesoscopic scale, at which the reinforcement architecture is defined, and the macroscopic scale, at which the structure is modeled. Most of the manufacturing defects impact the shape of the reinforcement and thus influences strains and damage evolution at the mesocopic scale [2, 3]. One of the main challenges in mesoscopic modeling of textile composites is to get a high quality finite element mesh (FEM) describing with accuracy the tow shapes and positions. The different methods of generating mesoscale models of textile composites are distinguished by their fidelity with the real material [4].

Reinforcement geometries based on analytical descriptions of the tow paths are well suited for parametric analyses of woven composite materials [5–7]. In these models, idealized tow paths and shapes are used. [7]. To improve generated tow shapes, analytical models can use experimental observations to identify the input parameters [8–10], or add mechanical regularization as in WiseTex based approaches [11–13]. While these methods are fast in generating virtual textile composites, the accuracy of the material representation is limited (inacurrate volume fractions or overestimated material strength) [3, 14]. Moreover, interpenetrations between tows are possible and have to be corrected before meshing (like, *e.g.,* in [7, 10]).

More accurate descriptions of woven reinforcements can be obtained from simulations of the manufacturing process [15–20]. However, the result is still an approximation of the real geometry. Furthermore, these approaches are based on an idealized description of the reinforcement that does not take into account variability of the reinforcement architecture or manufacturing defects.

Another method for producing meso-scale virtual textile composites, is to use non-destructive imaging of the material, especially micro-computed tomography (μCT).These

models provide a better representation of the variability of the textile structure and thus allow more accurate mechanical simulations [21]. In most of the published works, representative elementary volumes (REV) of woven composites are reconstructed from a CT-scan in two steps. In the first step, warp and weft tows are separated from each other. The second step consist of the individual labeling of the tows and the identification of the local fiber orientations.

Warp and weft tows can be separated manually [22], which is a tedious task if the weaving pattern is complex. Therefore, various automated CT-scan processing methods have been proposed. A common approach is to use the structure tensor [23, 24], which works well if the image contrast is high and the fibers can be seen individually. The required resolution can be reached with synchrotron X-rays or if the scanned volume is small enough, which for standard laboratory tomographs implies that it does not contain a full REV. At this scale, individual fibers can be tracked to reconstruct the fiber bundles composing the tows [25]. For lower resolutions and for images that present noise and low contrast, the structure tensor is inadequate for tow segmentation. If there is no fibrous pattern in the tows, the Gray Level Co-Occurence Matrix can be used [21]. Recent works have shown the benefits of machine learning algorithms with this process [26–28]. They can be applied to CT-scans with lower resolutions, because they consider larger features of the reinforcement, such as the yarns shapes and boundaries which are difficult to take into account with previously cited methods. On low contrast CT-images, Sinchuk et al. [26] obtained a more accurate segmentation with a machine learning algorithm than with previously cited methods. However, in order to implement this machine learning segmentation, a manual pre-segmentation is necessary to obtain the required training data. This step is the most time consuming for the user and the number of labelled images directly impacts the accuracy of the segmentation [26].

The labelling of the tows presents the challenge of identifying the contact zones between parallel tows. Topological information on the weaving pattern or the tow shapes may be needed [24, 29]. The difficulty of the problem increases with the number of contact zones, or the compactness of the reinforcement. A solution is to fit a parametrized description of the geometry to the tomography images using correlation [30, 31]. Global descriptors of

the textile architecture (like the relative positions of the tows) make these approaches less sensitive to the noise and therefore suitable at lower resolutions. However, convergence is only achieved if the initial model is already close to the real geometry, but even if a manual process may be necessary to determine the initial model, it can be less accurate and thus less labor-intensive compared to a complete manual segmentation. The computational cost is directly proportional to the size of the volume and to the number of parameters chosen to describe the geometry [30].

Creating high-quality conformal FE meshes of the generated geometries is a complex task [18]. The main difficulties lie in the multiple contact zones between tows and the sharp edges of the matrix pockets. These edges will prevent most meshing algorithms from converging. This problem can be circumvented by the inclusion of thin matrix layers between the tows, which makes the use of automated meshing tools possible [17, 32]. Nevertheless, small elements are required to mesh the thin matrix layers, which increases the mesh size and may induce low quality elements. Another solution is to keep a non-conformal mesh between the tows and apply tie constraints to transfer the mechanical loads between them [33]. Voxel meshes can easily be obtained even for very complex geometries. They are sufficient for the determination of the homogenized elastic behavior, but locally artificial stress concentrations are generated that may interfere with nonlinear phenomena such as damage initiation [34, 35].

In a recent work, octree-refined voxel meshes are smoothed to generate conformal meshes [36]. This technique provides an accurate description of the tow surfaces and reduces significantly the mesh size. Yet, the element size of the voxel mesh is kept on the tow surfaces, which leads to a large number of elements to accurately represent the geometry. Moreover, octree refinement is efficient if the meshed surface is small compared to the enclosed volume, which is not the case for thin tows.

In this article, a complete and mostly automated processing chain is presented to generate representative and realistic mesoscopic FE models of woven composite unit cells with or without defects. The approach is based on a segmentation procedure of μCT-scans, with a novel tow labeling and meshing method. Section 2 introduces the studied material and

presents the difficulties of processing the μCT-scans, which present ring artifacts and low contrast images. A strategy is proposed in section 3 to overcome these issues and to segment the matrix and the tow orientations. The tow labeling of the segmented REV is addressed in section 4. The resulting voxelized REV is smoothed, meshed and then coarsened using a technique proposed by Rassineux [37] (section 5), which allows for element quality control throughout the whole process. In section 6, the presented approach is applied to the material with defects.

2. Material

The material used in this work is a woven composite composed of a 5 harness satin weaving (5HS) of carbon fibers embedded in a thermoplastic PEEK matrix supplied by CETIM. The layup sequence is $[0/90]_{4s}$. The average ply thickness is 0.3 mm for a total thickness of 2.4 mm, and the unit cell (UC) size, which contains a full REV, is approximately 6.6×6.6 mm^2. Each tow contains 3k fibers. The material was scanned with a NSI X50 tomograph, with a source current of 100μA and a source voltage of 120kV. The reconstruction is based on 2200 projections (average of 20 frames taken at 7fps). Three contrast adjusted slices of the μ-CT are shown in Fig. 1b. The total scanned volume of $25 \times 20 \times 2.4$ mm^3 limits the voxel size to 7μm. The reinforcement geometry is identified on a sub-volume of 1.2 times the UC size, corresponding to 1286x1286x307 voxels. The cell size was chosen in order to treat the tomography with a regular laptop (Macbook Pro with 8Gb RAM). In Fig. 1b we can see that despite the low resolution, the identification of the tow orientation can be identified based on the fibrous texture visible in the in-plane slices. It is easier to identify the tow boundaries on in-plane images rather than on through-thickness slices. Therefore, the in-plane slices of the REV were processed during the segmentation.

The signal to noise ratio (SNR) provides a good descriptor of the image quality. For both matrix and tows this ratio is below 4. In photography, a minimum SNR of 10 is considered an acceptable image quality [38]. The gray level distibution of the whole CT-scan (Fig. 1c) shows a significant overlap between the ranges of the matrix and the tows, which makes segmentation by thresholds difficult. Another issue of the tomography is the presence of ring

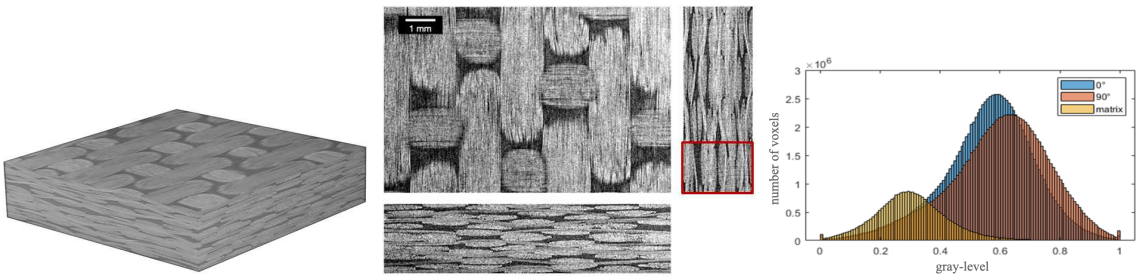

(a) (b) (c)

Figure 1: (a) CT-scan of the material, (b) details of in-plane and through-thickness slices, (c) gray level distribution of the whole CT-scan

artifacts. These are CT hardware related and inherent to the detector calibration. They emerge as circular lines in the images that interfere with the fiber texture. In our case the ring artifacts are parallel to the weft tows. They are visible in the red rectangle in the through-thickness cross-section normal to the weft direction (Fig. 1b).

The ring artifacts in our images prevent the processing of the tomography with a conventional algorithm based on the structure tensor, which is computed at each pixel of the image $I(x, y)$ by:

$$T = K_\sigma * \begin{bmatrix} (\nabla_x I)^2 & \nabla_x I \nabla_y I \\ \nabla_x I \nabla_y I & (\nabla_y I)^2 \end{bmatrix} \tag{1}$$

where $\nabla_x I$, $\nabla_y I$ are the image gradients along the x and y axes, respectively. The application of a Gaussian convolution K_σ of standard deviation σ makes the structure tensor less sensitive to noise. The eigenvector of the structure tensor associated to its maximum eigenvalue corresponds to the main texture orientation. The coherence, computed with the eigenvalues ($\lambda_1 > \lambda_2$), gives a confidence indicator of the direction given by the structure tensor.

$$Coh = \frac{\lambda_1 - \lambda_2}{\lambda_1 + \lambda_2} \tag{2}$$

In case of a unidirectional texture ($\lambda_1 > 0$ and $\lambda_2 = 0$) the coherence reaches its maximum of $Coh = 1$, for an isotropic texture ($\lambda_1 = \lambda_2$) it is $Coh = 0$.

Fig. 2b shows the orientation obtained with the structure tensor calculated on an in-plane slice of the CT-scan. The texture quality in the image leads to inaccurate orientations

especially in the warp tows. Even after binarizing the orientation map by a threshold at 45°, the result is not satisfying (Fig. 2d). During the scan, the specimen is rotated around the weft direction (90°). Ring artifacts appear in the warp tows as light lines oriented parallel to the weft tows. As a result, there are two perpendicular line textures in the warp tows. For a more accurate segmentation, directional filtering is needed as shown in section 3.

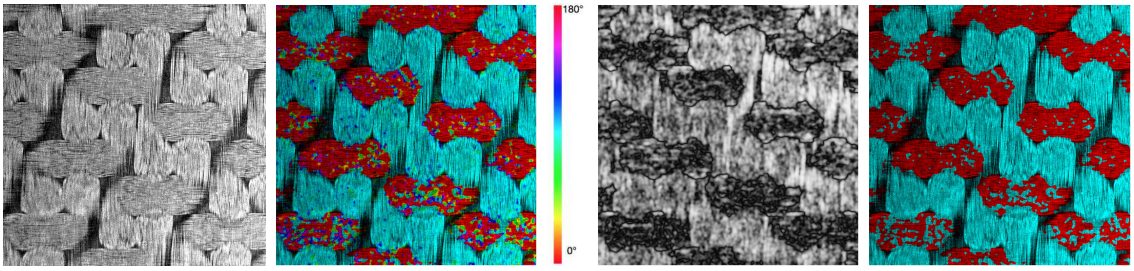

(a) (b) (c) (d)

Figure 2: (a) In-plane slice of the CT-scan, (b) orientation map obtained with the structure tensor, (c) coherence, (d) binarized orientation map.

3. Segmentation of the tow orientations

The first step of the proposed segmentation procedure is to separate the matrix from the tows. In-plane slices of the CT-scan are processed one by one. The CT-scan image 2a presents an illumination gradient that prevents the use of a single gray level threshold to segment the matrix. Chen et al. [39] considered the illumination gradient as a low-frequency variation of the gray level of the image. They applied a filter based on the discrete cosine transform (DCT) to correct the illumination. The result obtained with this method is shown in Fig. 3a. The corrected image is then binarized at an optimum threshold determined with the Otsu method (Fig. 3b). Due to the overlap between the gray level distributions of the tows and the matrix (Fig. 1c), not only the pixels associated with the matrix are selected. The segmented image is therefore cleaned by a sequence of operations. First, the holes smaller than 300 pixels are removed in the segmented image and its complement. Then a disk kernel of 2 pixels is used to do a morphological dilation of the image, followed by a gaussian blur (with a sigma of 2 pixel) and a binarization. Finally, the result presented in

Fig. 3c is obtained after repeating the hole removal with the same parameters as in the first step.

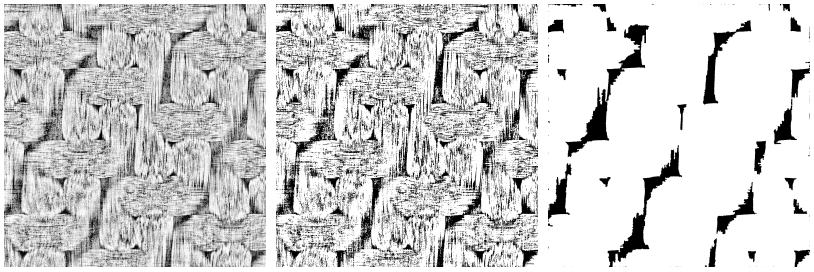

(a) (b) (c)

Figure 3: (a) Result of the illumination correction using DCT filtering, (b) binarized image, (c) segmented matrix after cleaning operations.

To separate the warps (0°) and the wefts (90°), a directional filtering is implemented to deal with the ring artifacts presented in section 2. The aim is to segment one of the two orientations accurately. The second one can then be determined by complementarity with the matrix. The real part of a Fast Fourier transform (FFT) of the image in the frequency domain is shown in Fig. 4a. The two main tow orientations appear as two clearer lines. The 90° orientation is then filtered from the image using the mask shown in Fig. 4b (white=0, black=1), as it corresponds to the direction of the ring artifacts in the in-plane slices. An inverse FFT transforms the image back to the spatial domain (Fig. 4c). As a result, the ring artifacts are removed from the warp tows, while the texture of the weft tows becomes isotropic noise. As the coherence for an isotropic texture is close to 0 whereas for a unidirectional texture it is close to 1, this choice of filtering maximizes the difference in coherence between the two orientations. The pixels belonging to the warp tows are then those with coherence above a threshold determined with the Otsu method. The pixels belonging to the weft tows are the remaining pixels that are neither warp nor matrix. The result for one in-plane slice is presented in Fig. 4d.

Filtering the orientation with the warp tows instead would not remove the artifacts, which in this case would be perpendicular to the filtered direction. The result would be a noisy texture with artifacts for the warp tows and an untouched weft texture, which would

yield a significantly smaller difference in coherence.

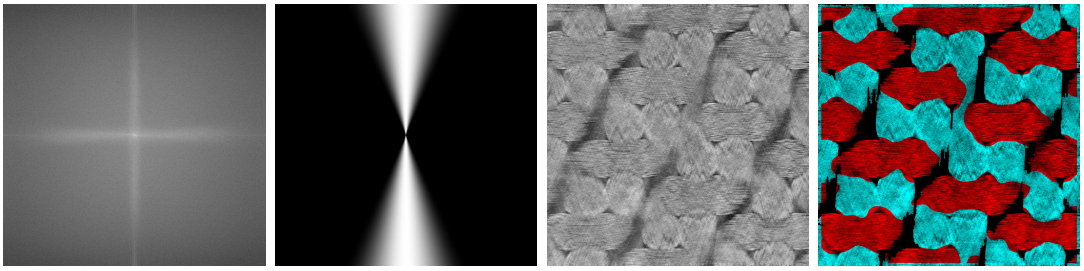

(a) (b) (c) (d)

Figure 4: (a) FFT of an in-plane slice of the tomography in the frequency domain, (b) directional filtering mask, (c) slice of the tomography after filtering, (d) result of the segmentation with directional filtering.

After segmenting the in-plane slices one by one, they are assembled to reconstruct the 3D REV. The through-thickness section of the reconstructed REV shown in Fig. 5b evidences some remaining segmentation errors. In some zones, the texture quality is so degraded that the directional filtering gives an incorrect segmentation. This is the case for example at the bottom left corner of Fig. 5b, which is the closest to the center of rotation of the specimen during the CT-Scan (red dot). These zones have to be corrected by contouring manually the faulty zone in several cross-sections. They cover less than 0.5% of the total volume. The visual verification of the segmentation and the manual correction takes less than 20 minutes. Then a post-processing step is applied to correct the smaller topological inconsistencies, which are mainly small included volumes of an incorrect phase visible as white areas in the gray tows in Fig. 5b. The cleaning is a 2D iterative process in the 3 directions. In each iteration, for each class (weft, warp, and matrix) the inclusions are detected and filled automatically with the corresponding material. The result of the corrections is shown in Fig. 5c. Treating the constituent materials separately in this process avoids the removal of small matrix pockets. This step corrects 0.02% of the total volume after 3 iterations and removes all the visible inclusions.

Since the in-plane slices are segmenting independently, small discontinuities between neighboring slices can appear. A 3D Gaussian filter with a standard deviation of 1.5 pixels is applied to smooth the outlines of the tows and to remove the discontinuities. The result

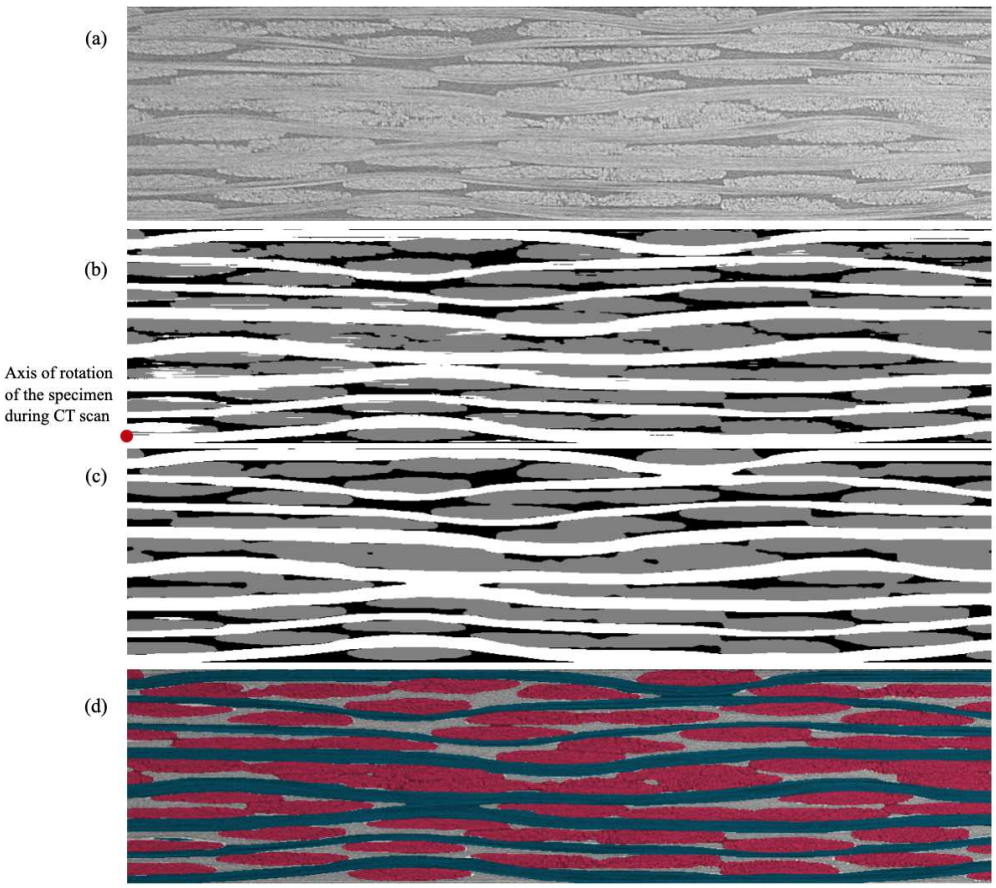

Figure 5: (a) Through-thickness section of the tomography, (b) result of the segmentation with directional filtering, (c) result after manual correction and cleaning, (d) final segmentation superposed to the tomography image.

after all cleaning steps is shown in Fig. 5c. The segmentation quality can be assessed visually in Fig. 5d. The tows superpose well with the tomography image and their shapes are well respected. The full segmented REV is presented in Fig. 6.

Visually comparing the shapes of the tow cross-sections between the segmentation and the CT-scan gives a first qualitative validation. For a more quantitative comparison, a reference volume or "ground truth" (GT) is determined by manual segmentation of the tomography. Usually, tomographies of woven composites are segmented manually by interpolating the tow surfaces between tow cross-section contours traced manually on several through-thickness slices. However, due to the low image quality, the tow cross-section boundaries

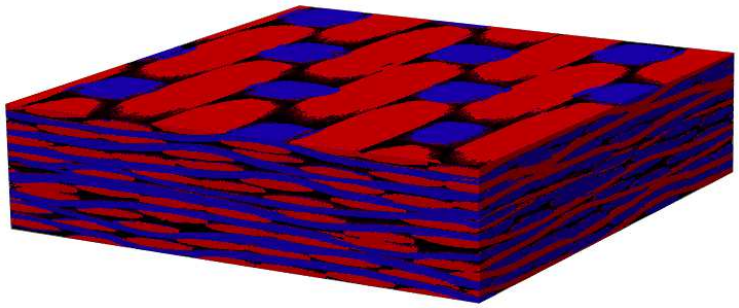

Figure 6: Final segmented 3D REV.

are not clear enough to be precisely followed manually, as shown in section 2. The manual segmentation is therefore carried out on the in-plane slices of the REV. Each slice is segmented making the process long but more accurate. A Gaussian filter is then applied on the resulting volume to smooth the contours of the tows.

The quality of the segmentation is quantified by the confusion matrix presented in Table 1. It presents the overlapping of the predicted classes with the manually segmented reference. The presented segmentation approach tends to overestimate the volume of the matrix in the REV. This is a consequence of the overlapping of the gray-level ranges shown in Section 2. The studied material contains the same amount of warp and weft tows. However, the presented segmentation method yields a lower volume fraction of weft tows compared to the warp tows. This difference is caused by the directional filtering process, which mainly impacts the weft direction. It induces a slight loss of sharpness of the tow edges, which adds to the edge smoothing induced by the regularization term used to compute the coherence. This slightly reduces the tow cross-sections leading to an overestimation of the matrix volume fraction. The warp orientation, which is extracted by the directional filtering, is slightly oversegmented. Therefore, the weft direction, which is deduced by subtracting the matrix from the complement of the warp tows, is underestimated. Despite this difference in volume fraction, the shape of the tows is respected as shown in Fig. 5, which was the main goal of our approach.

The volume fractions only give a global indication of the segmentation quality. In order to analyse the geometric accuracy locally, the edges of 9 tows are segmented manually on

(%)	Matrix in SA	Weft in SA	Warp in SA	Total Vf in GT
Matrix in GT	11.2	0.4	0.7	12.3
Weft in GT	4.1	36.4	3.3	43.8
Warp in GT	2.5	0.3	41.1	43.9
Total Vf in SA	17.8	37.1	45.1	

Table 1: Confusion matrix for the segmentation approach (SA). The reference used for the comparison is the manual segmentation (ground-truth : GT).

20 slices in each of the two orientations. The cross-sections are used to extract geometric features of the tows (area, width, thickness). This operation is realised on the automatically segmented volume and on the manually segmented reference. The statistic analysis of these features is presented in Fig. 7a. As expected, the area of the weft tow cross-sections is smaller in the automatically segmented volume (median about 17% lower). Accordingly, the area of warp tows is slighty larger (median increased by 3,5%). The trends are the same for the width and the thickness of the tows with a decrease of 12.2% and 6% respectively. The differences in volume fractions thus correspond to a global shrinking of weft tows, and a sligth inflation of warp tows compared to the reference model.

4. Separation of parallel tows

In the case of small contact zones, the tows can be separated by identifying isolated tow sections and by joining these sections across the contact zones [29]. Another possibility is to determine the planes between the plies by analyzing the matrix distribution in the REV [40]. This plane is then used to identify the contact zones between tows belonging to different plies. Separating tows of the same ply is simple if the contact area is small, as for example in a plain weave architecture [40]. In the segmented REV obtained in section 3, there are more than 1000 distinct large contact zones. Hence, there are only very few isolated sections of tows, which are insufficient for labeling. Moreover, in the material with defects, the plies cannot be separated by planes due to the out-of-plane waviness introduced by the defects.

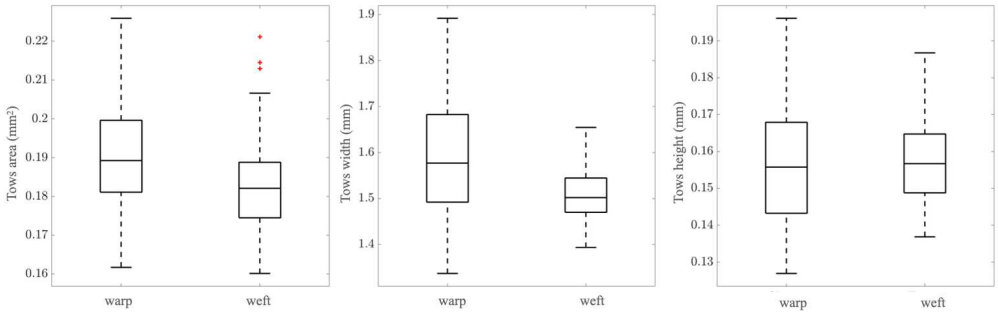

(a) Manual segmentation

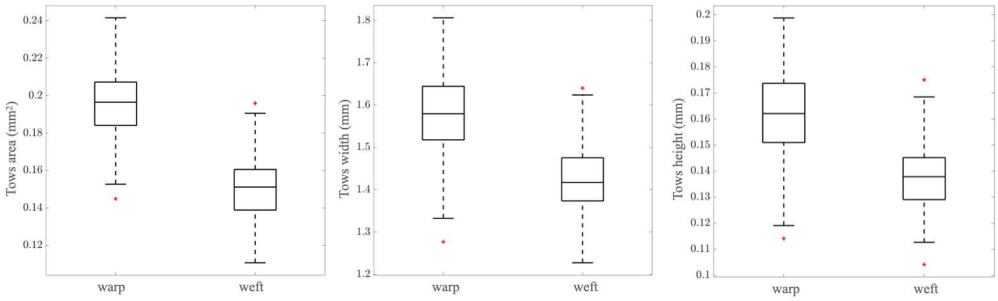

(b) CT-Scan segmentation

Figure 7: Geometrical variability measured in the CT-scan (a) compared to the variability measured on the segmented volume (b).

In Fig. 8 the strategy used to separate parallel tows is presented. The first main step is to retrieve the center line of the tows by a combination of tracking and fitting. Then, these lines are inflated within the pre-segmented geometry in order to determine the contact zones between tows and to label each voxel of the REV.

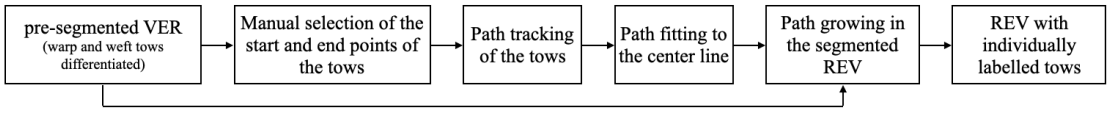

Figure 8: Diagram of the separation process of parallel tows.

To separate the tows, the first step in our process is to retrieve the center path of each tow. This can be done manually by pointing the centers of several cross-sections. However, this operation is time-consuming on a full REV, which contains 140 tows in our case. In order to trace these paths automatically, we use the distance transform on curved space

(DTOCS) algorithm [41], which was originally developed to find the shortest route between two points on a 2D gray-level height map. We implemented the DTOCS algorithm in 3D. In order to reduce the cost of computing the distance transform map, each tow is tracked individually in a box of 3 tows width by 3 tows height centered at the midpoint between the two seeds points used for the tracking. As the algorithm is designed for following the path of the smallest gradient, the matrix and the perpendicular tows are filled with a white noise that increases the gradient. In this way, we ensure that the tracked path stays in the desired tow. The transition between the noise and the inner part of the tow is smoothed by a Gaussian convolution, which increases the robustness of the tracking and further pushes the path towards the tow center. An example of this process is presented in the Fig. 9a,b.

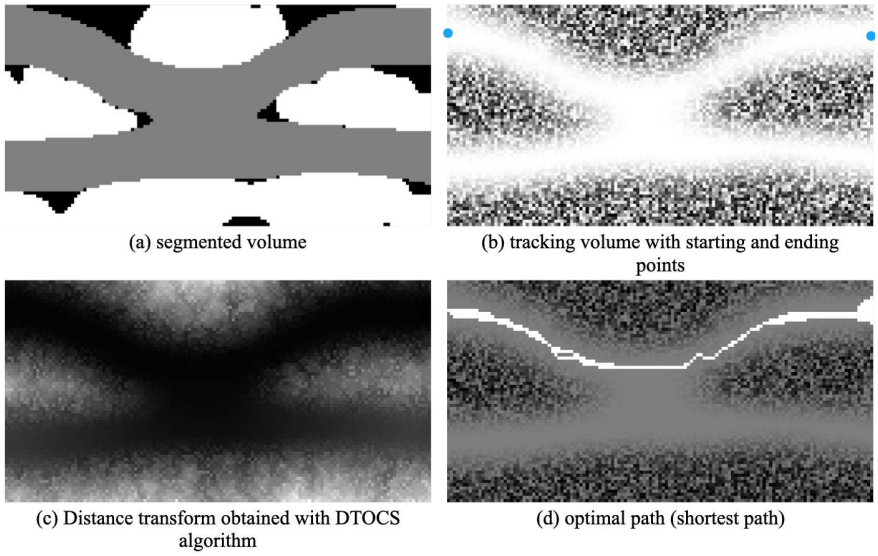

Figure 9: Example of implementation of the tow tracking steps with the DTOCS algorithm on a simplified 2D model.

The seed points are the manually determined tow centers on each side of the REV. Corresponding starting points on opposite sides of the REV are identified based on the assumption that the topology (the relative position of the tows compared to each other) is the same on both sides. Each tracking of tows is performed independently, and only the start point of the considerd tow are kept (blue dots on Fig. 9b).

The DTOCS algorithm yields the shortest path through the tows. A distance map is

computed based on the gray-levels and the distance between adjacent voxels (Fig. 9c). This map represents, in each voxel, the length of the shortest path between the two end points through the considered voxel. The shortest path shown in Fig. 9d is obtained by selecting in the distance map all the voxels with the minimum value. The algorithm accurately tracks 95% of the tows. However, in the weft direction between the two symmetric center plies, some tracking errors occur, because the contact between tangent tows can be 4 times longer than the tow width in this zone. It is therefore possible that the tracking algorithm finds a shorter path that passes from one tow into another one. These specific paths (6 of the 140 tows) have to be manually corrected by pointing the center of the tows on several cross-sections within the incorrectly tracked zone and interpolating the path over the REV. This operation takes approximately 10 min. The final result is shown in Fig. 10.

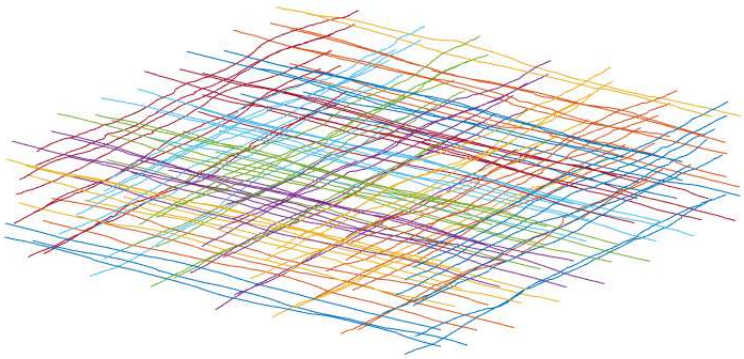

Figure 10: Tracked weft and warp tow paths.

Since the obtained shortest paths do not correspond with the center lines of the tows, they are adjusted by fitting circles to rescaled cross sections of the tows. To do so, the in-plane dimensions of the REV are reduced by a factor of 8.7, which is equal to the average ratio between tow width and thickness in the studied material. This rescaling operation leads to tow cross sections that are approximately circular (Fig. 11a). Fig. 11b shows the tracked tow paths in the rescaled REV surrounded by circles of a diameter equal to the average diameter of the tow cross sections in Fig. 11a. The positions and radii of the circles are then adjusted by minimization of a cost function

$$f(\boldsymbol{x}) = e_{corr}(\boldsymbol{x}) + w_{inter} e_{inter}(\boldsymbol{x}) \tag{3}$$

where e_{corr} is similarity error calculated using the Jacquard index between the mask of the idealized circular cross-sections and the segmented slice. e_{inter} is a penalizing term to control interpenetration, which corresponds to the percentage of pixels within the circles that belong to more than one circle. w_{inter} is the weight of the interpenetration correction in the optimization process, which is set to 2 for our case. The result for one slice of the rescaled REV is shown in Fig. 11c. A similar approach was used by Benezech in order to fit an analytical model to a CT-scan [30].

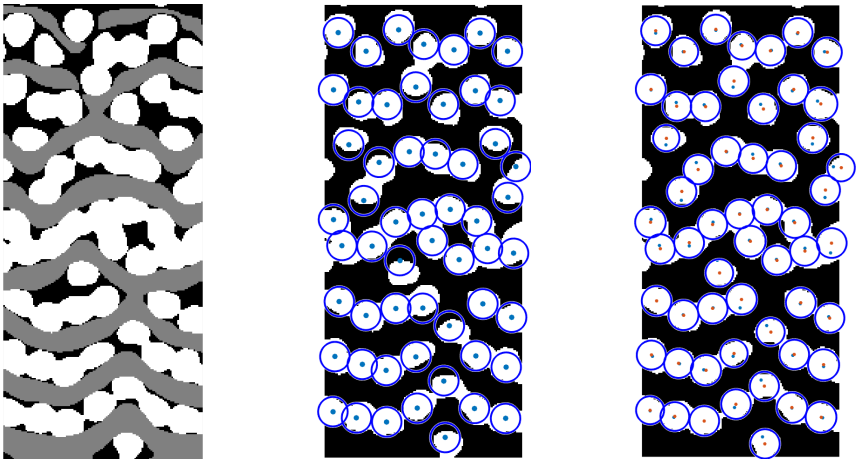

(a) (b) (c)

Figure 11: (a) Rescaled segmented slice of the REV, (b) tracked tow paths with initial average circles, (c) best fitting circles with their centers in red next to the tracked tow paths in blue.

This procedure is repeated on every fifth slice of the tomography in both warp and weft direction, as a compromise between computational cost and precision. The center line of each tow is then obtained by spline interpolation. The coordinates are then rescaled to the initial REV size.

The center lines are used as starting points of an inflation procedure to fill the REV with labeled tows. To accelerate the procedure, the resolution of the voxel mesh is reduced by a factor of 4 in the in-plane directions and by a factor of 2 through the thickness. This reduces the 470M voxels of the initial REV to 14M. To each voxel V in the coarse grid, we assign the constituent material with the highest number of voxels in V in the fine grid. Through

the following steps the voxels are considered cubic despite the anisotropic size reduction of the volume. The initial ratio of the volume is recover at the end of the mehing procedure.

We suppose that the shapes of the tow cross sections are approximately elliptical (which is confirmed by the approximately circular cross sections in the rescaled REV shown in Fig. 11a), and that the deviations are mainly caused by contact interactions with adjacent tows. The inflation process is therefore based on elliptical cross sections with half axes a and b that are normal to the main direction of the tow (warp or weft). The values of a (1.5mm) and b (0.16mm) are obtained from measurements of the tow width and thickness, respectively, on several slices of the CT-scan. The ellipses are discretized in steps of 0.1 times the voxel size. Likewise, the splines interpolating the tow center lines are also discretized in steps of 0.1 times the voxel size. This gives a regular grid of an idealized tow surface with a constant elliptical cross section. The tows are inflated by iteratively increasing an inflation ratio e starting from 0 in increments of 0.01 (illustrated by Fig. 12a). At each iteration step, for each tow surface grid point, it is checked in which voxel it is located (Fig. 12b). If the voxel has not yet been assigned to a material, it is attributed to the current tow. If the voxel is already assigned to a material, the inflation process is stopped for the respective point on the surface grid (see Algorithm 1). The inflation ratio is increased simultaneously for all tows up to a maximum value of $E = 110\%$. This accounts for the fact that if a tow is constrained by the contact with another tow in some direction (the inflation is stopped in this direction), the fibers are redistributed in other directions where there is no contact with other tows (the inflation continues for $e > 1$ in these directions).

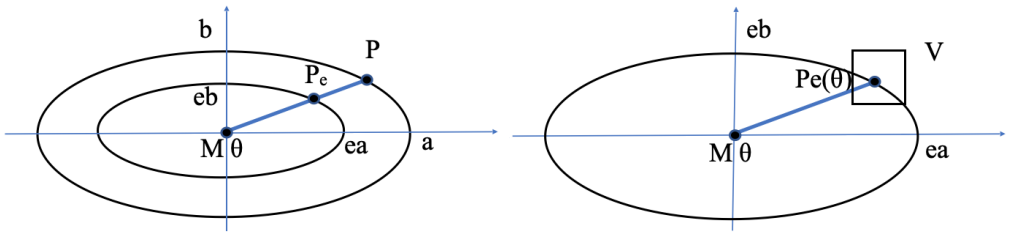

(a) (b)

Figure 12: Schematization of the inflation process.

Algorithm 1: Inflation procedure

Initialize an empty voxel array, no material yet is assigned ;
Define complementary voxels (matrix, weft/warp) as assigned ;
Define the maximum inflation ratio E ;
while $e < E$ **do**
  foreach *tow* I **do**
    foreach *point* M *of the spline* **do**
      Define the ellipse of half axes ea, eb ;
      foreach *point* $P_e(\theta)$ *of the ellipse* **do**
        Determine the voxel V *which contains the point* ;
        if V *is unassigned* **then**
          Assign V *to tow* I
        else
          Disable the inflation process at point M *for direction* θ ;

Note that no complex intersection procedure is applied in this algorithm. A tow surface grid size of less than 0.2 times the voxel size is sufficient to ensure the robustness of the filling process. The procedure is applied to voxel arrays pre-filled with the respective complement, *i.e.,* the warp tows are inflated with the voxels that during the segmentation process were identified as belonging to the matrix or to the weft tows treated as already assigned. The inflation thus stops as soon as a weft tow or a matrix pocket is encountered. Likewise, the weft tows are inflated with the warp and matrix voxels already treated as assigned. This limits the growth of the tows to their actual dimension observed in the tomography images, and the simultaneous growth of all tows leads to a correct identification of the contact zones between parallel tows.

5. Meshing procedure

The generated voxel mesh is then smoothed using the method developed by Rassineux [37]. It is based on a modified Catmull-Clark subdivision technique and converts the voxel

mesh into an unstructured tetrahedral mesh, which allows for mesh quality during the voxel deformation. During the smoothing process, a minimum angle between two adjacent element faces of 20° is imposed, which avoids the presence of flat elements in the final mesh. The smoothing is carried out using the reduced voxel mesh in order to limit the computational costs. When returning to the original scale of the CT-scan, the resulting minimum angle between element faces is 8.2°. In the studied case, the smoothing combined with the rescaling of the REV increases the volume fraction of the tows by about 4%. This difference increases with the minimum angle. The value was thus chosen as a compromise between mesh quality and respecting the tow shape.

After smoothing, the volume fraction of the matrix in the REV is 16.3%, which is much closer to the real value (see Table 1). The volume fraction of the tows increases accordingly to 38.0% for the warp and 45.7% for the weft tows. The meshing step doesn't impact significantly the volume fraction inside the REV. The variation of the volume fraction mesured before and after the meshing is less than 1%. The tow shapes are well preserved, because the node displacement during the smoothing process is less than the size of a voxel. Some details of the smoothed REV are shown in Fig. 13.

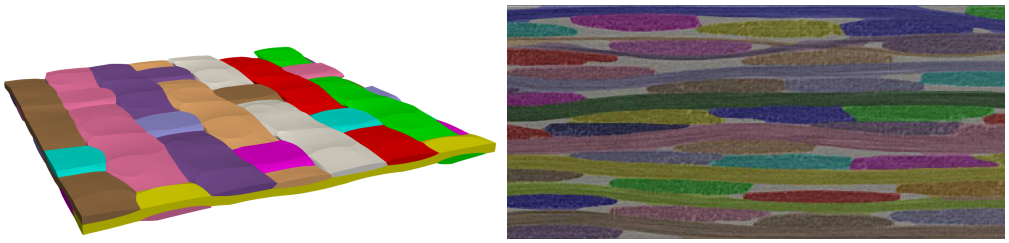

(a) (b)

Figure 13: (a) Smoothed ply, (b) through-thickness section of the final mesh after smoothing superposed to the CT-scan.

After smoothing, the mesh contains 18.4M nodes and 105.5M elements. Only 0.3M elements have a quality below 0.1. The quality is measured for a tetrahedron as the ratio of the inscribed sphere of the element to the longest edge times a coefficient chosen such that an equilateral element has a quality of 1. The mesh is then coarsened using the algorithm

developed by Rassineux [37]. The final mesh is composed of 1.1M nodes and 6.5M elements, *i.e.,* a reduction by a factor of 16.5. The number of elements with a quality between 0.1 and 0.3 is 4313 and there is no element below this quality. The final coarsened mesh is presented in Fig. 14. The low quality elements are distributed over different locations in the mesh and not necessarily found in areas where the geometry is complex, such as in thin matrix layers as could be expected. In order to ensure the convergence of the 3D mesh generator, new points must be added to solve configurations known as Schönhardt polyhedron, especially when the local volume to mesh is non-convex and lower quality elements may be created [42].

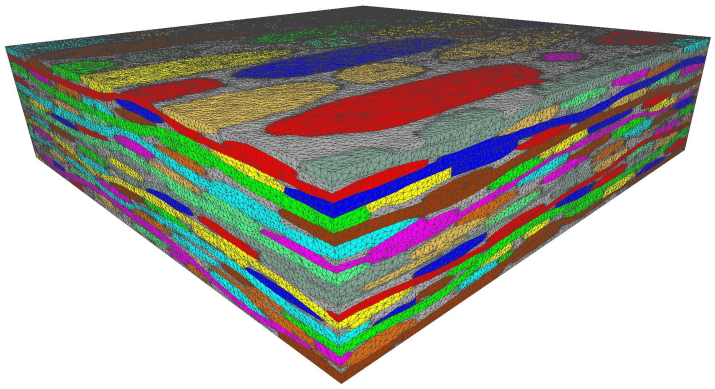

Figure 14: Final coarsened mesh of the REV

6. Application to the material with defects

The presented approach is designed to work with local tow disorientations (blue box in Fig. 15a) as induced by the specific manufacturing process of the material. This process also causes tow splitting as highlighted in red in Figs. 15a and 15b.

The segmentation procedure described in section 3 does not need to be modified. The path tracking algorithm (section 4) has to be adapted to deal with the split tows. These tows have to be identified by visually inspecting the tomography. In these tows, two distinct

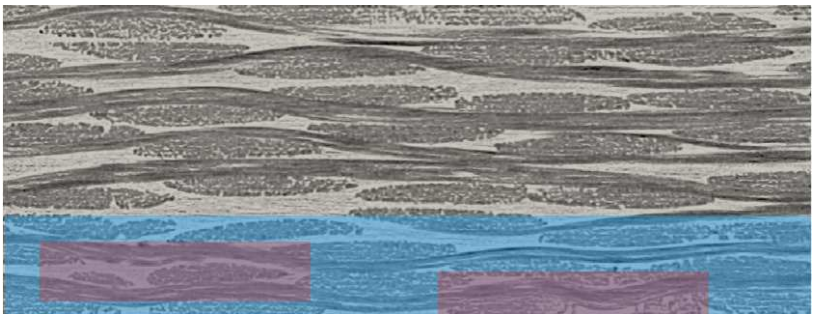

(a)

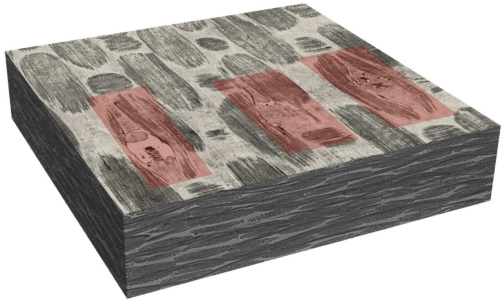

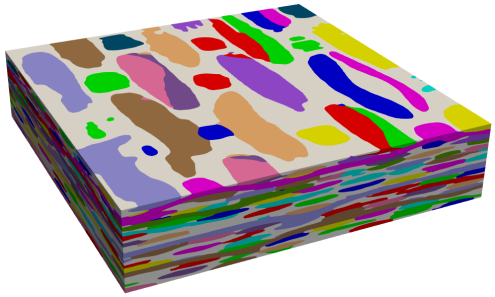

(b) (c)

Figure 15: (a),(b) CT-scan of the material with defect highlighted, tow disorientations in blue, tow splitting in red (c) model of the material with defect generated with our approach

paths are introduced by placing two starting points in the same tow on each side of the REV. If one tow half undulates much more than the other, the tracking algorithm will follow the straighter half for both paths. In the studied volume, two split tows (4 paths in total) require the same manual intervention as presented in section 4 to correct the paths and to obtain a correct representation of the topology with the defects.

The split tows are composed of two strands of different sizes, which is accounted for in the inflation algorithm 1 by multiplication of the inflation ratio r_i with the respective size ratio. The strands grow thus at the same speed as the rest of the tows. The coefficient is determined by measuring the strand width on several sections througout the split zone. The resulting mesh is presented in Fig. 15c and some details of through-thickness slices are superposed to the corresponding CT-images in Fig. 16.

The presented approach deals with the tow orientation defects in the studied material without any problem. In fact, the defect introduces an out-of-plane displacement of less

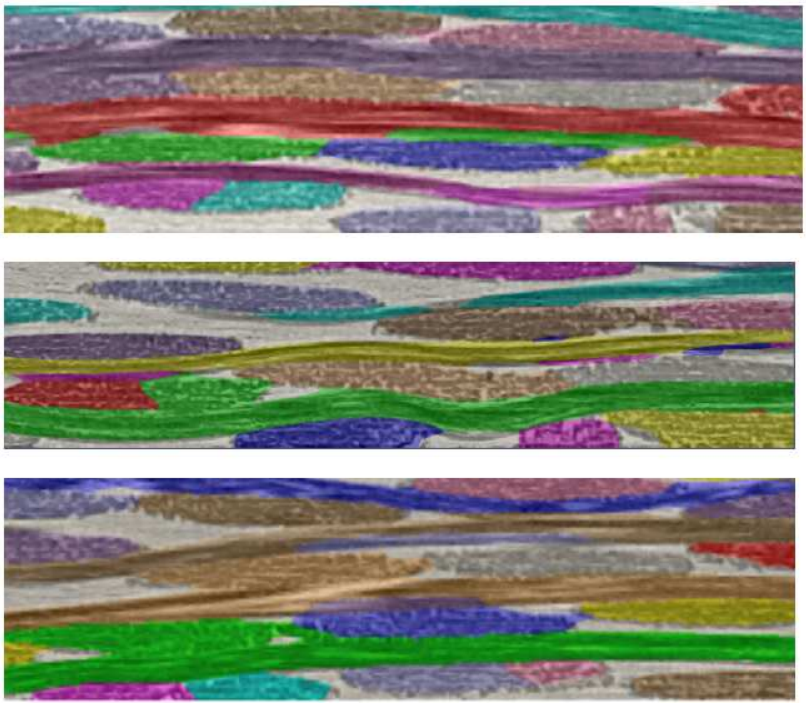

Figure 16: Detail of the mesh overlapped with the CT-scan

than the thickness of two plies, which does not cause an important modification of the tow curvature. However, tow splitting implies a topological modification of the reinforcement architecture and the tow tracking has to be adapted and some additional manual corrections are needed in order to deal with it. On the other hand, tow splitting is a very specific defect of the manufacturing process of the studied material, which are rarely found in usual textile composites.

7. Conclusion

In the proposed approach, the process of generating mesoscopic REV models of composites with woven reinforcements has largely been automated. The approach is not optimized for computational cost. The segmentation process takes about 30 minutes and the tracking about 3 hours. Both steps can be implemented in parallel, which would significantly accelerate the processing time. However, the meshing and the coarsening algorithms are implemented in parallel and take about 2 hours for the studied REV. The manual input on

the reinforcement topology is limited to a minimum. Only the centers of the tows have to be indicated on the 4 sides of the volume. The main challenge was to process low quality CT-scans with reconstruction artifacts. The ring artifacts are handled by directional filtering. However, the tow texture close to the rotation axis during the CT-scan is too degraded for the proposed method. Manual correction of the tow segmentation is required in these degraded areas of the REV. The work requires less than 20 minutes compared to more than ten hours for a full manual segmentation of the REV.

The tow path tracking also needs some manual correction in some critical areas where parallel tows share a large contact zone. This is the case for 6 out of the 140 tows of the REV. In the case of geometries with fewer contacts, the approach should require even less corrections. The time-consuming manual definition of the reinforcement geometry usually required for geometrical models is avoided. The tow labeling and the meshing are fully automated and do not require any action of the user.

Due to the directional filtering during the segmentation process, the volume fraction of the tows that are not affected by the ring artifacts is slightly increased with respect to the precise manual segmentation. Furthermore, smoothing operations to deal with the low contrast and noise correction reduce the tow cross sections and thus lead to a significant overestimation of the matrix volume fraction. However, the shapes of the tows are correctly determined and superpose well with the CT-images. The smoothing processes used to generate a conformal mesh from the segmented voxel representation compensates to some extent the overestimation of the matrix volume fraction. In mechanical simulations, the quantity of fibers in a tow is known and the local fiber volume fraction has to be adapted to the local tow cross section. In this way, the effect of small variations of the tow volume fractions on the mechanical behavior can be compensated as long as the tow shapes, undulations, and their topology are correctly represented. The fully automated meshing algorithm transforms the voxel mesh into a conformal tetrahedral mesh while avoiding flat elements. High quality elements for accurate mechanical simulations are thus ensured.

The presented approach is able to deal with tow orientation defects as long as the topology of the reinforcement is not significantly impacted, which was not the case with the studied

material. Likewise, the tow undulations in the studied weaving are not an issue. However, the approach was not tested on composites with 3D woven reinforcements. If there are tows that are oriented locally almost in the through-thickness direction, the inflation process will have to be adapted. Also, the current approach already needs some manual corrections if the tow paths are incorrectly tracked trough parallel tows with large contact areas. In 3D weavings, where due to the high tow waviness some tow parts may be significantly longer than the parts of other tows in the same zone, this may become an issue as the tracking algorithm always chooses the shortest path. Therefore, in the case of 3D weavings with large contact zones between parallel tows, the number of manual corrections of the tow tracking may increase considerably.

The segmentation of split tows requires some adaptations of the algorithm, such as double path tracking for the split tows. The split tows have therefore to be identified by visual inspection of the tomography and taken into account when placing the starting points for the tow tracking on the REV sides. The tow splitting defect is very specific to the manufacturing defect of the studied material.

This application shows that the approach is designed for continuous reinforcements. Tow breaks or ply drops cannot be treated without adaptations. Furthermore, as the approach is based on the analysis of the fibrous texture of the tows, it has to be visible in the CT-images (which is the case in our images taken with a standard laboratory tomograph). However, scans taken with even lower resolutions without any fibrous texture in the tows cannot be treated with the presented approach without significant adjustments.

8. Declaration of interest

The authors declare that they have no known competing financial interests or personal relationships that could have appeared to influence the work reported in this paper.

References

[1] O. Rozant, P. E. Bourban, J. A. E. Månson, Drapability of Dry Textile Fabrics for Stampable Thermoplastic Preforms, Composites Part A: Applied Science and Manufacturing 31 (11) (2000) 1167–1177.

[2] S. D. Green, M. Y. Matveev, A. C. Long, D. Ivanov, S. R. Hallett, Mechanical Modelling of 3D Woven Composites Considering Realistic Unit Cell Geometry, Composite Structures 118 (2014) 284–293.

[3] L. F. Varandas, G. Catalanotti, A. R. Melro, B. G. Falzon, On the Importance of Nesting Considerations for Accurate Computational Damage Modelling in 2D Woven Composite Materials, Computational Materials Science 172 (2020) 109323.

[4] T. Gereke, C. Cherif, A Review of Numerical Models for 3D Woven Composite Reinforcements, Composite Structures 209 (2019) 60–66.

[5] A. C. Long, L. P. Brown, 8 - Modelling the Geometry of Textile Reinforcements for Composites: TexGen, in: P. Boisse (Ed.), Composite Reinforcements for Optimum Performance, Woodhead Publishing Series in Composites Science and Engineering, Woodhead Publishing, 239–264, 2011.

[6] H. Lin, X. Zeng, M. Sherburn, A. C. Long, M. J. Clifford, Automated Geometric Modelling of Textile Structures:, Textile Research Journal .

[7] A. Wendling, J. L. Daniel, G. Hivet, E. Vidal-Sallé, P. Boisse, Meshing Preprocessor for the Mesoscopic 3D Finite Element Simulation of 2D and Interlock Fabric Deformation, Applied Composite Materials 22 (6) (2015) 869–886.

[8] G. Hivet, P. Boisse, Consistent 3D Geometrical Model of Fabric Elementary Cell. Application to a Meshing Preprocessor for 3D Finite Element Analysis, Finite Elements in Analysis and Design 42 (1) (2005) 25–49.

[9] S. Yan, X. Zeng, L. Brown, A. Long, Geometric Modeling of 3D Woven Preforms in Composite T-joints:, Textile Research Journal .

[10] R. G. Rinaldi, M. Blacklock, H. Bale, M. R. Begley, B. N. Cox, Generating Virtual Textile Composite Specimens Using Statistical Data from Micro-Computed Tomography: 3D Tow Representations, Journal of the Mechanics and Physics of Solids 60 (8) (2012) 1561–1581.

[11] S. V. Lomov, A. V. Gusakov, G. Huysmans, A. Prodromou, I. Verpoest, Textile Geometry Preprocessor for Meso-Mechanical Models of Woven Composites, Composites Science and Technology 60 (11) (2000) 2083–2095.

[12] I. Verpoest, S. V. Lomov, Virtual Textile Composites Software WiseTex: Integration with Micro-Mechanical, Permeability and Structural Analysis, Composites Science and Technology 65 (15) (2005) 2563–2574.

[13] B. Wintiba, B. Sonon, K. Ehab Moustafa Kamel, T. J. Massart, An Automated Procedure for the Generation and Conformal Discretization of 3D Woven Composites RVEs, Composite Structures 180 (2017) 955–971.

[14] R. D. B. Sevenois, D. Garoz, F. A. Gilabert, S. W. F. Spronk, S. Fonteyn, M. Heyndrickx, L. Pyl, D. Van Hemelrijck, J. Degrieck, W. Van Paepegem, Avoiding Interpenetrations and the Importance

of Nesting in Analytic Geometry Construction for Representative Unit Cells of Woven Composite Laminates, Composites Science and Technology 136 (2016) 119–132.

[15] N. Isart, B. El Said, D. S. Ivanov, S. R. Hallett, J. A. Mayugo, N. Blanco, Internal Geometric Modelling of 3D Woven Composites: A Comparison between Different Approaches, Composite Structures 132 (2015) 1219–1230.

[16] Y. Wang, X. Sun, Digital-Element Simulation of Textile Processes, Composites Science and Technology 61 (2) (2001) 311–319.

[17] F. Stig, S. Hallström, Spatial Modelling of 3D-woven Textiles, Composite Structures 94 (5) (2012) 1495–1502.

[18] G. Grail, M. Hirsekorn, A. Wendling, G. Hivet, R. Hambli, Consistent Finite Element Mesh Generation for Meso-Scale Modeling of Textile Composites with Preformed and Compacted Reinforcements, Composites Part A: Applied Science and Manufacturing 55 (2013) 143–151.

[19] Y. Mahadik, S. R. Hallett, Finite Element Modelling of Tow Geometry in 3D Woven Fabrics, Composites Part A: Applied Science and Manufacturing 41 (9) (2010) 1192–1200.

[20] D. Durville, Simulation of the Mechanical Behaviour of Woven Fabrics at the Scale of Fibers, International Journal of Material Forming 3 (2) (2010) 1241–1251.

[21] N. Naouar, E. Vidal-Salle, J. Schneider, E. Maire, P. Boisse, 3D Composite Reinforcement Meso F.E. Analyses Based on X-ray Computed Tomography, Composite Structures 132 (2015) 1094–1104.

[22] H. Bale, M. Blacklock, M. R. Begley, D. B. Marshall, B. N. Cox, R. O. Ritchie, Characterizing Three-Dimensional Textile Ceramic Composites Using Synchrotron X-Ray Micro-Computed-Tomography, Journal of the American Ceramic Society 95 (1) (2012) 392–402.

[23] N. Naouar, E. Vidal-Sallé, J. Schneider, E. Maire, P. Boisse, Meso-Scale FE Analyses of Textile Composite Reinforcement Deformation Based on X-ray Computed Tomography, Composite Structures 116 (2014) 165–176.

[24] V. Mazars, O. Caty, G. Couégnat, A. Bouterf, S. Roux, S. Denneulin, J. Pailhès, G. L. Vignoles, Damage Investigation and Modeling of 3D Woven Ceramic Matrix Composites from X-ray Tomography in-Situ Tensile Tests, Acta Materialia 140 (2017) 130–139.

[25] R. M. Auenhammer, L. P. Mikkelsen, L. E. Asp, B. J. Blinzler, Automated X-ray computer tomography segmentation method for finite element analysis of non-crimp fabric reinforced composites, Composite Structures 256 (2021) 113136.

[26] Y. Sinchuk, P. Kibleur, J. Aelterman, M. N. Boone, W. Van Paepegem, Variational and Deep Learning Segmentation of Very-Low-Contrast X-ray Computed Tomography Images of Carbon/Epoxy Woven Composites, Materials 13 (4) (2020) 936.

[27] M. A. Ali, Q. Guan, R. Umer, W. J. Cantwell, T. Zhang, Deep learning based semantic segmentation

of micro-CT images for creating digital material twins of fibrous reinforcements, Composites Part A: Applied Science and Manufacturing 139 (2020) 106131.

[28] S. Blusseau, Y. Wielhorski, Z. Haddad, S. Velasco-Forero, Instance segmentation of 3D woven fabric from tomography images by Deep Learning and morphological pseudo-labeling, Composites Part B: Engineering 247 (2022) 110333.

[29] C. Chapoullié, J.-P. D. Costa, M. Cataldi, G. Vignoles, C. Germain, Orientation-Guided Two-Scale Approach for the Segmentation and Quantitative Description of Woven Bundles of Fibers from Three-Dimensional Tomographic Images, Journal of Electronic Imaging 24 (6) (2015) 061113.

[30] J. Bénézech, G. Couégnat, Variational Segmentation of Textile Composite Preforms from X-ray Computed Tomography, Composite Structures 230 (2019) 111496.

[31] A. Mendoza, J. Schneider, E. Parra, E. Obert, S. Roux, Differentiating 3D Textile Composites: A Novel Field of Application for Digital Volume Correlation, Composite Structures 208 (2019) 735–743.

[32] S. V. Lomov, D. S. Ivanov, I. Verpoest, M. Zako, T. Kurashiki, H. Nakai, S. Hirosawa, Meso-FE Modelling of Textile Composites: Road Map, Data Flow and Algorithms, Composites Science and Technology 67 (9) (2007) 1870–1891.

[33] S. Jacques, I. De Baere, W. Van Paepegem, Application of Periodic Boundary Conditions on Multiple Part Finite Element Meshes for the Meso-Scale Homogenization of Textile Fabric Composites, Composites Science and Technology 92 (2014) 41–54.

[34] A. Doitrand, C. Fagiano, F. X. Irisarri, M. Hirsekorn, Comparison between Voxel and Consistent Meso-Scale Models of Woven Composites, Composites Part A: Applied Science and Manufacturing 73 (2015) 143–154.

[35] N. V. De Carvalho, S. T. Pinho, P. Robinson, Reducing the Domain in the Mechanical Analysis of Periodic Structures, with Application to Woven Composites, Composites Science and Technology 71 (7) (2011) 969–979.

[36] M. Y. Matveev, L. P. Brown, A. C. Long, Efficient Meshing Technique for Textile Composites Unit Cells of Arbitrary Complexity, Composite Structures 254 (2020) 112757.

[37] A. Rassineux, Robust Conformal Adaptive Meshing of Complex Textile Composites Unit Cells, Composite Structures 279 (2022) 114740.

[38] Photography — Digital Still Cameras — Determination of Exposure Index, ISO Speed Ratings, Standard Output Sensitivity, and Recommended Exposure Index, Standard, ISO, 2019.

[39] W. Chen, M. J. Er, S. Wu, Illumination Compensation and Normalization for Robust Face Recognition Using Discrete Cosine Transform in Logarithm Domain, IEEE Transactions on Systems, Man, and Cybernetics, Part B (Cybernetics) 36 (2) (2006) 458–466.

[40] Y. Sinchuk, P. Kibleur, J. Aelterman, M. N. Boone, W. V. Paepegem, Geometrical and Deep Learn-

ing Approaches for Instance Segmentation of CFRP Fiber Bundles in Textile Composites, Composite Structures 277 (2021) 114626.

[41] L. Ikonen, P. Toivanen, Shortest Routes on Varying Height Surfaces Using Gray-Level Distance Transforms, Image and Vision Computing 23 (2) (2005) 133–141.

[42] E. Schönhardt, Über die Zerlegung von Dreieckspolyedern in Tetraeder., Mathematische Annalen 98 (1928) 309–312.